ROYAL SOCIETY OF CHEMISTRY

PERSPECTIVE

CrossMark
← click for updates

Hybrid strategies and technologies for full spectrum solar conversion

P. Bermel,*[ab] K. Yazawa,[a] J. L. Gray,[b] X. Xu[a] and A. Shakouri[a]

Harvesting the full spectrum of sunlight using a hybrid approach offers the potential for higher efficiencies, lower power production costs, and increased power grid compatibility than any single technology by itself. In this article, the base technologies for converting sunlight into electricity, including photovoltaics and solar thermal approaches are discussed. Then feasible strategies for combining them to utilize the various portions of the solar spectrum most effectively are discussed. In this study, we particularly focus on the advantages of a spectral splitting approach. This helps to convert higher energy photons (UV and visible) directly into electrons using optimized single or tandem photovoltaic (PV) cells, while capturing lower energy photons as heat using a selective solar absorber, which absorbs photons within a range of energies, down to a cutoff in the mid-infrared. The solar heat is then thermally concentrated and driven through a high temperature thermoelectric generator on top of a high efficiency mechanical engine (e.g., a steam-driven Rankine cycle) through a heat exchanger, which connects to both thermal storage and the mechanical engine at 550 °C. The thermal storage allows for significant flexibility in the time of power generation (also known as dispatchability) at a modest cost. Hence, the system can produce power for hours after sunset. Ideally, the system can achieve efficiencies over 50% using a combination of an InAlAs/InGaP tandem photovoltaics, $ErAs:(InGaAs)_{1-x}(InAlAs)_x$ thermoelectrics, and mechanical Rankine cycles. The configuration and operating conditions can be optimized to minimize the levelized cost of energy (LCOE).

Broader context

To help reduce dependence on fossil fuels, there have been an increasing range of efforts to develop technologies to harvest solar energy in an economical fashion. The cost of solar harvesting systems is driven by several key factors: the efficiency of power conversion, the lifetime and reliability of its components, and the cost of the raw materials and any fabrication/construction required. Individual solar power conversion technologies have recently emerged, notably photovoltaics and solar thermal, which each have performance limits well below fundamental thermodynamic limits, driven by losses inherent to different parts of the spectrum, while none of these technologies can convert the whole spectrum. Thus, it is feasible and desirable to split the solar spectrum to utilize each technology over its optimal wavelength range. In this article, promising approaches to combining two or more of these individual technologies are discussed. In particular, it is shown that using high-energy solar photons for photovoltaics and medium-energy solar photons for thermoelectrics with bottoming Rankine cycle has potential to achieve 50% solar-to-electricity conversion using existing materials. Also, over 50% of the harvested energy goes to thermal storage for the generation after sunset, which could enable highly efficient baseload solar power generation throughout each day.

1. Introduction

Thanks to recent innovations in the design and manufacturing of photovoltaic (PV) modules, supported by large research & development (R&D) programs such as the US Department of Energy SunShot, the affordability and importance of solar power has been rapidly growing. PV is already a $100 billion industry, accounting for only a small fraction of worldwide power generation now, but a much greater fraction of new installations. For example, penetration in California alone has already exceeded 3%.[1] However, three key challenges present significant barriers to further adoption on a utility scale. First, the recent, rapid cost reductions are projected to slow considerably with consolidation of the industry, thus limiting the number of markets in which grid parity would be rapidly achieved. The average selling prices of solar modules dropped 80% in five years and have just started to level off in the last two years. Second, photovoltaic cells convert solar energy directly into electricity, but are limited by basic physics in their conversion efficiencies to the

[a] Birck Nanotechnology Center, Purdue University, 1205 West State St., West Lafayette, IN 47907, USA. E-mail: pbermel@purdue.edu
[b] School of Electrical and Computer Engineering, Purdue University, 465 Northwestern Ave., West Lafayette, IN 47907, USA

so-called Shockley–Queisser limit of 31% for a single junction. In practice, this limits the maximum power density for space-constrained applications. Third, the lack of dispatchability associated with PV can cause large daily swings in solar power generation. This effect has created major challenges for utilities in tying a highly variable energy source into the grid. Even the 5% penetration of PV in Germany can yield peak power generation over 20% of the grid in the middle of a sunny, summer day. This unfortunately results either in slowdowns of baseload power plants (even though they are not designed to do this) or more commonly, dumping of surplus solar energy. Unfortunately, even the creation of a new incentive of 660 euros per MW per h for energy storage in Germany has not been sufficient to alleviate this dispatchability challenge.

In order to overcome the problems associated with solar PV as it is currently practiced, there is a great need for a new paradigm for solar power generation. Under this new approach, the system will be designed with inexpensive storage in mind from the beginning, thus heading off the dispatchability challenge at the pass. Also, all the individual power-generating components would be compatible with solar conditions and be based on well-established technologies, to achieve affordability, reliability, and scale. Furthermore, this new paradigm will be designed for ultra-high efficiencies, thus overcoming the challenges that have plagued previous generations of dispatchable solar generation, such as concentrated solar thermal power.

In this paper, we develop the intellectual case for a utility-scale photovoltaic/thermoelectric/mechanical (PV/TE/ME) hybrid approach depicted in Fig. 1 that brings together three distinctive power-generating components with their own strengths and weaknesses, using each in the best way possible in order to achieve remarkably high system-level exergies. Other approaches previously studied include hybrid PV/TE systems, which can generate electricity from waste heat in PV modules,[2–5] as well as thermovoltage-combined solar-powered water splitting, which has been shown to generate hydrogen suitable for storage.[6] In the PV literature, it is well-known that only stacked multijunctions and spectral splitting[7–9] have been shown to exceed the single junction Shockley–Queisser limit in experiment. Thus, our plan is to use both concepts, plus a thermal cycle for the lowest energy photons, since it is more effective than a low-bandgap PV cell. Thus, the key components of this system are tandem III–V lattice-matched epitaxially grown PV cells, and on the thermal side, thermoelectrics, and a mechanical engine (e.g., a thermal Rankine cycle).

The key to the performance of the system is to create an early, sharp spectral split between the photovoltaic and thermal components of the system, and to efficiently convert the incoming sunlight into electron–hole pairs or heat, respectively. The advantages of spectral splitting are as follows. First, it removes the current-matching condition present in stacked multijunctions. Second, it removes the requirement for lattice matching between the adjacent cells. Third, it is less sensitive to spectral conditions (i.e., changes in relative humidity). Finally, and most importantly, spectral splitting reduces the photon entropy compared to other approaches. For unconcentrated AM1.5 sunlight under standard
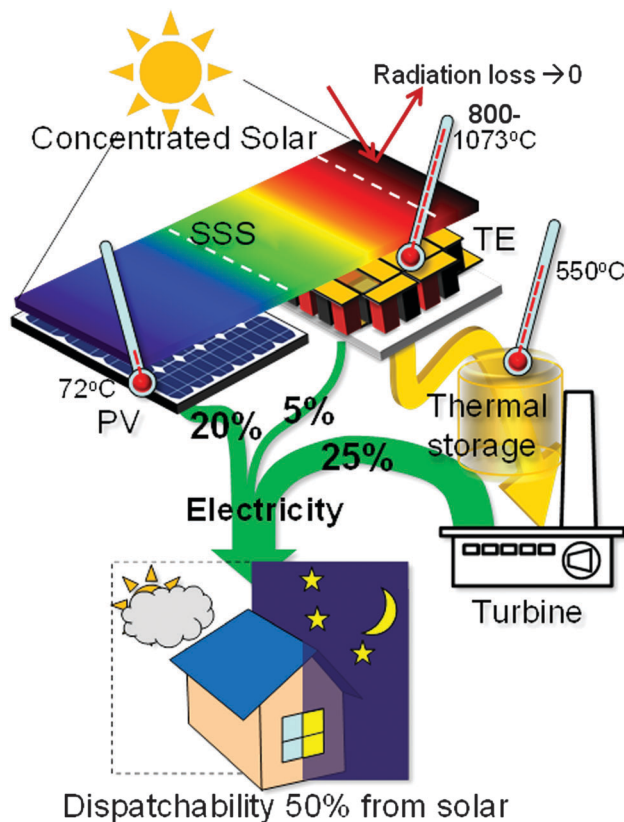

Fig. 1 Our hybrid concept for generating electricity from solar power: concentrated sunlight is stored and converted via photovoltaics (PV), thermoelectrics (TE) and mechanical engines (ME) to achieve 50% conversion efficiency.

conditions, this has been shown to increase the theoretical maximum efficiency by approximately 5%.[10] The promise of spectral splitting has been dampened by the potential costs of expensive dichroic filters and possible failure modes.[7] Still, recent studies have shown that innovative manufacturing approaches based on large-area deposition of inexpensive materials may achieve cost-effective spectral splitting with a small number of layers,[8] which could simultaneously reduce the chance of delamination, thus increasing the lifetime of these filters significantly.[9]

In this paper, we show that there are significant advantages to using solid-state thermoelectrics in topping cycle applications with moderate to high thermoelectric figures of merit, ZT ∼ 0.5–3. This is because there is high amount of entropy lost between filtered thermal radiation (not absorbed by the PV) and the working fluid (steam) in the mechanical Rankine cycle engine. Thermoelectrics can convert a small amount of this energy into useful work, and yet all of the "waste" heat transported to the cold side of the TE module can still do work if the thermal impedance is matched with the high temperature heat exchanger. As summarized in Fig. 2, our calculations show that this approach is capable in principle of achieving 50% exergy and 50% dispatchability on a utility scale, including realistic losses in optical concentration and collection, as well as PV conversion, solar thermal absorption, and conduction
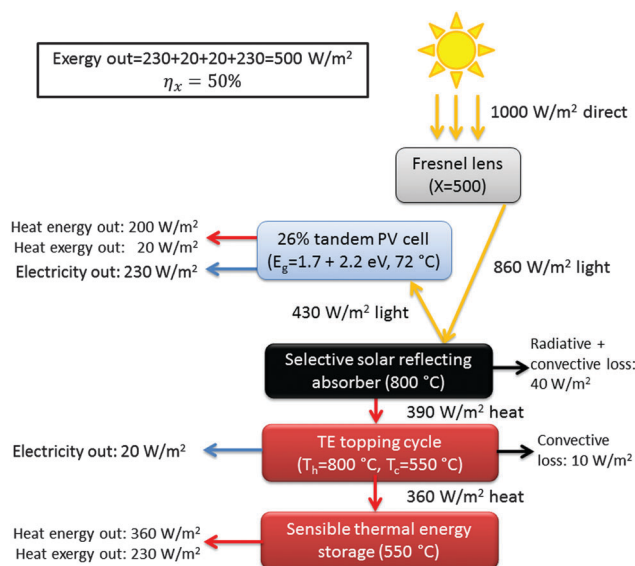
Fig. 2 Block diagram providing the details of the energy flow (in terms of yellow photons, red phonons, and blue electrons), specific-ally calculated for our PV/TE/ME hybrid system illustrated in Fig. 1.
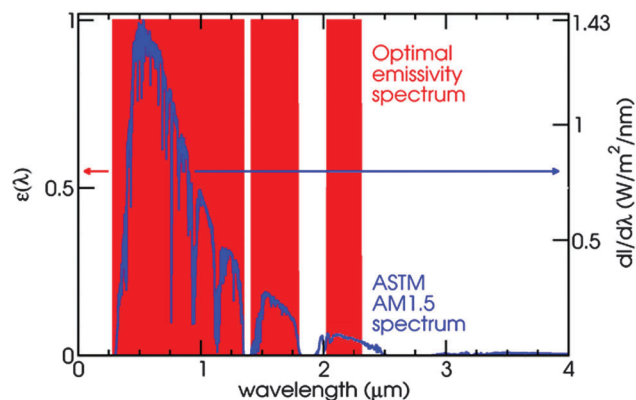

Fig. 3 Comparison of an ideal solar absorption spectrum, illustrated in red, with the AM1.5 solar spectrum in blue. Most overlap occurs for visible and near-IR wavelengths (adapted from ref. 24).

and convective losses. The projected installed cost of this system is $0.73 per W_x without subsidies, which is well below the current cost of installed, non-dispatchable PV systems (approximately $2 per W_x with subsidies), and even below the SunShot goal for 2020 of $1 per W_x. This system would provide an ideal solution for utility-scale deployment compatible with the utility grid that is capable of reducing fossil fuel dependence and pollution while also saving consumers money. While the focus of this paper is on utility scale dispatchable electricity generation, the key components (solar PV, SSAR, TE) can also be used in distributed microgrid applications to provide both electricity and hot water to buildings. The efficiency for electricity generation will be lower since Rankine cycles don't scale as well and there are increased thermal losses (increased surface to volume ratio). However, if there is use for hot water (from concentrated solar cell cooling or the waste heat from Rankine cycle), the overall exergy of the system could be quite high.

In the rest of the paper, we first review existing solar conversion technologies (Section 2), and then we consider how to combine them properly in a novel fashion for highly efficient, dispatchable performance (Section 3). We then conclude with a summary of our key results, as well as a perspective on future work (Section 4).

2. Enabling solar conversion technologies

2.1. Concentrating solar photovoltaics

Multijunction solar cells have demonstrated efficiencies of over 40% at concentration.[11] Single and multijunction solar cells can further benefit from solar concentration, which has led to demonstrations of the highest independently-validated efficiencies.[11] Thermally stable dye-sensitized solar cells represent a lower

cost alternative.[12] In this context, there is also potential to utilize novel mechanisms for recovering low energy photons, such as upconversion[13] and energy filtering.[14] We will employ this same spectrum splitting strategy in this hybrid system by utilizing the high energy photons in the PV component of the system while directing the lower energy photons to the TE and thermal storage components. It has been shown that the wide band gaps in a multijunction solar cell are the major contributors to the overall PV efficiency.[15] Thus, by utilizing only the high energy photons in the PV component, the overall efficiency of the hybrid system can be improved. Further, by keeping the PV component from direct contact with the thermal components that must be maintained at a very high temperature, we avoid the efficiency losses due to the operation of the PV devices at high temperature.[16]

Both single junction and tandem (dual) junction solar cells will be modelled, but it is expected that the tandem configuration will result in the highest hybrid system efficiency. The efficiency of a multijunction solar cell can be written as[17]

$$\eta_{\text{tandem}} = \eta_{\text{ultimate}}\eta_{\text{photon}}\left[\beta_1\frac{V_{\text{OC},1}}{E_{\text{G},1}}\text{IQE}_1\text{FF}_1 + \beta_2\frac{V_{\text{OC},2}}{E_{\text{G},2}}\text{IQE}_2\text{FF}_2\right],$$

(1)

where η_{ultimate} is the ultimate efficiency as defined by Shockley and Queisser,[18] η_{photon} is the efficiency with which photons are generated (this includes losses due to reflection and non-absorption), β_i is a weighting factor based on the relative number of photons absorbed in that junction,[19] and IQE is the overall internal quantum efficiency of the absorbed photons. The open-circuit voltage of each junction is derived from a model describing the junction saturation current for a "state-of-the-art" fabricated cell.[20] For any number of series-connected junctions, the current at the maximum power point (and hence the fill factor of each junction) can be obtained from:[21]

$$J_{\text{MP}} = \frac{\sum_{i=1}^{N}\left[nkT\ln\left(\frac{J_{\text{SC},i} + J_{0,i} - J_{\text{MP}}}{J_{0,i}}\right) - R_{\text{S},i}J_{\text{MP}}\right]}{\sum_{j=1}^{N}\left(R_{\text{S},i} + \frac{nkT}{J_{\text{SC},i} + J_{0,i} - J_{\text{MP}}}\right)},$$

(2)

which can then be solved numerically to arbitrary precision using the bisection method. A multidimensional unconstrained nonlinear minimization method can then be used to find the band gaps that produce the highest efficiency under the given constraints[22] (e.g., atmospheric/spectral conditions or operating temperatures).

2.2. Concentrating solar thermal conversion

The balance between absorption and reflection in our selective solar surfaces is driven by basic physics. It is well known from Planck's law of blackbody radiation that the peak wavelength of a blackbody spectrum scales inversely with temperature. Since the sun's surface can be considered to be at a temperature of approximately 5500 °C, and any realistic terrestrial application will involve much lower temperatures than that, a significant gap opens up between the regimes in which high and low absorptivity and emissivity are needed. If we restrict ourselves to a short-wavelength regime with unit emissivity and a long-wavelength regime with zero emissivity, the ideal wavelength at which such a transition between the two should occur will depend on the exact operating temperature and solar optical concentration employed. For example, a selective solar absorber in unconcentrated sunlight operating at 400 °C with a perfect sharp ideal cutoff wavelength of 1.775 μm, will capture 92.8% of incoming sunlight as heat (assuming no other losses).

In order to quantify the limits of performance of selective solar surfaces, we must define a quantity we call the thermal transfer efficiency η_t, which is the fraction of sunlight captured as heat at a particular temperature T and solar optical concentration C:[23]

$$\eta_t = B\bar{\alpha} - \frac{\bar{\varepsilon}\sigma T^4}{CI_s},$$ (3)

where B is the window transmissivity (if present), $\bar{\alpha}$ is the spectrally averaged absorptivity, $\bar{\varepsilon}$ is the spectrally averaged emissivity, σ is the Stefan–Boltzmann constant, and I_s is the solar intensity, generally taken as 1 kW m^{-2}. However, in thermal equilibrium, absorptivity and emissivity both depend on the emissivity spectrum of the absorber, which allows us to rewrite the thermal transfer efficiency as follows:[24]

$$\eta_t = \frac{1}{I_s}\int_0^\infty d\lambda \varepsilon(\lambda)\left\{B\frac{dI}{d\lambda} - \frac{2\pi hc^2}{C\lambda^5[\exp(hc/\lambda kT) - 1]}\right\}$$ (4)

In this form, it is clear that for every wavelength, the quantity in curly braces in the above equation will be either positive or not. For positive values, we would like the emissivity to be as large as possible (i.e., one), while for negative values, we would like the emissivity to be as small as possible (i.e., zero). Typically, this corresponds to a step-function in emissivity from one to zero at a cutoff wavelength that falls somewhere in the solar spectrum. Fig. 3 shows the optimal emissivity as a function of wavelength superimposed on the AM1.5 solar spectrum for an exemplary concentration of 500 Suns, held at 1000 K. Only wavelengths where the power of concentrated sunlight exceeds the emission of a blackbody at 1000 K are fully absorbed; the remaining wavelengths are reflected back into space.
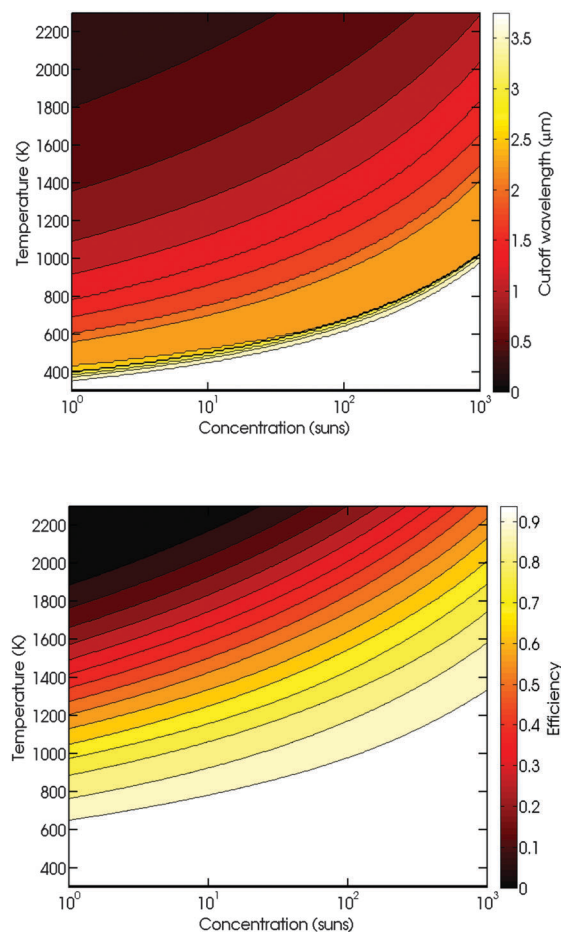

Fig. 4 Key properties of ideal selective solar absorbers: (top) ideal cutoff wavelength; and (bottom) maximum thermal transfer efficiency (adapted from ref. 24).

In Fig. 4 (top), we show the optimal cutoff wavelength as a function of the operating temperature and solar concentration. A distinct trend becomes apparent, where higher concentrations and lower operating temperatures lead to longer wavelength cutoffs, while the opposite conditions lead to shorter wavelength cutoffs. Along similar lines, Fig. 4 (bottom) shows the thermal transfer efficiency as a function of operating temperature and solar optical concentration. Higher concentrations and lower operating temperatures lead to high thermal transfer efficiencies, and the opposite conditions lead to much lower thermal transfer efficiencies – all the way down to 0%.

On the other hand, the maximum conversion efficiency possible for any system converting thermal energy into electricity is the so-called Carnot efficiency η_c, given by:

$$\eta_c = 1 - T_c/T_h$$ (5)

where T_h is the temperature of the initial heat input, while T_c is the temperature of the cold heat sink.

Thus, there is an inherent tension between efficiently harvesting sunlight as heat, and efficiently converting that heat to electricity. As a result, a system-level approach is often required to maximize the performance of the overall energy
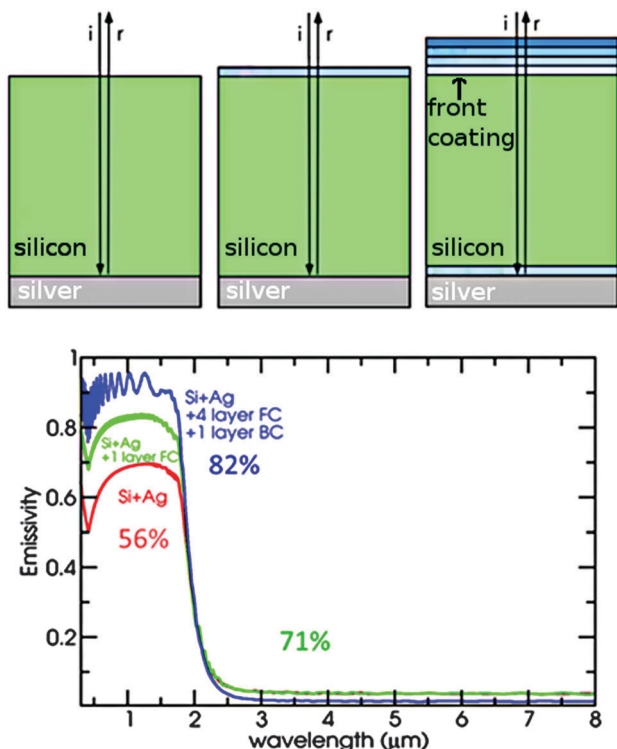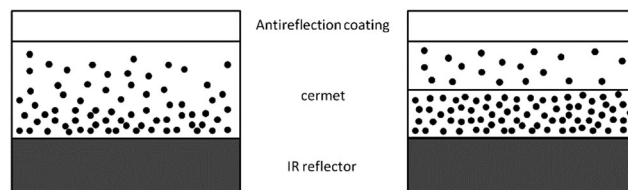
Fig. 6 Schematic of a cermet with a graded metal concentration (left) and a double cermet composed of low and high metal volume fraction layers (right).

Fig. 5 Semiconductor Selective Solar Absorbers at $T = 700$ °C and 100 Suns. (top) 3 silicon/silver selective solar absorbers with 1–4 front coating (FC) and 0–1 back coating (BC) layers; (bottom) optimal emissivity curves for each design, along with overall thermal transfer efficiencies. Adapted from ref. 26.

conversion process. Such an analysis has been explored in recent literature.[23–26]

Semiconductor materials are generally transparent for frequencies below their electronic bandgap, but absorb strongly at higher frequencies. If a semiconductor is placed on a metal, short wavelength solar radiation in the visible region will be absorbed by the semiconductor layer, while long wavelength radiation will pass through the semiconductor, and get reflected back by the metal layer.[27] Depending on the operating conditions, a wide variety of semiconductors may be suitable for selective solar absorbers, including silicon, germanium, and lead sulfide. Due to the high refractive index found near the band edge of most semiconductors, which creates unwanted reflection for frequencies above the bandgap, an antireflection coating is generally added to suppress reflection and thus enhance performance.

Donnadieu et al.[28] considered a silicon/germanium tandem absorber placed on a silver reflector with an anti-reflection coating in front, consisting of four layers of transparent dielectrics with refractive indices varying from 1.43 to 2.79. Optimization via simulation yielded spectrally-averaged absorptivity of $\bar{\alpha} = 0.89$ and spectrally-averaged emissivity $\bar{\varepsilon} = 0.0389$ at 300 °C and $\bar{\varepsilon} = 0.0545$ at 500 °C. Okuyama et al. in 1980[29] used an amorphous silicon absorber with an aluminium reflector, and an anti-reflection coating consisting of SiO_2/TiO_2. This selective absorber had $\bar{\alpha} = 0.79$–0.81 and $\bar{\varepsilon} = 0.12$–0.14 at 400 °C. In 2010, Bermel et al.[26] numerically optimized a larger class of selective

solar absorbers under two sets of conditions. For unconcentrated sunlight ($C = 1$) at an absorber temperature $T = 400$ K, a germanium absorber and silver reflector with optimized front and back coatings showed $\bar{\alpha} = 0.907$ and $\bar{\varepsilon} = 0.016$ at 400 K (Fig. 5), with a thermal transfer efficiency of 0.881. For concentrated sunlight ($C = 100$) at an absorber temperature, $T = 1000$ K, silicon actually has an appropriate bandgap. Combining hot silicon at 1000 K with a silver back reflector and multilayer front and back coatings yields $\bar{\alpha} = 0.868$ and $\bar{\varepsilon} = 0.073$, for a thermal transfer efficiency of 0.822. The efficiency drops with increasing temperature, as the blackbody spectrum starts to overlap more closely with that of the sun.[26]

Ceramic–metal composite coatings, also known as cermets, consist of nanoscale metal particles embedded in a ceramic matrix. A cermet selective solar absorber consists of an antireflection layer, one or more cermet layer(s), and a reflective substrate. The cermet acts as the primary absorber, while the reflective substrate, usually made from the same metal used in the cermet layer(s), helps to minimize absorption of undesired infrared wavelengths. Cermet designs have a high degree of flexibility. Their solar selectivity can be optimized by varying metal and ceramic constituent elements, nanoparticle coating materials and thickness, as well as nanoparticle concentration, shape, size, and orientation.[30] Good candidates for the cermet constituents are metals with high melting points such as Cu, Au, Ni, Mo, Cr, Co, Pt, and W, and dielectrics such as oxides of the preceding compounds, along with SiO_2, Al_2O_3, and MgO. Among these, the most widely used selective coatings, due to their low cost, are black chrome, a graded $Cr–Cr_2O_3$ cermet, and nickel-pigmented anodic Al_2O_3. In other work, Sathiaraj et al. in 1989[31] optimized a single layer cermet composed of $Ni:Al_2O_3$ with homogeneous metal volume fraction of 0.61 on nickel coated glass and experimentally measured $\bar{\alpha} = 0.94$ and $\bar{\varepsilon} = 0.07$ at 100 °C. It was stable up to 500 °C in vacuum.

A single homogeneous cermet film does not usually show extremely high solar selectivity by itself since the absorption of the cermet causes an impedance mismatch with the antireflection coating. Thus, more complex structures with a more gradual change in absorption have also been investigated. A first candidate is a graded cermet whose metal concentration gradually decreases from the bottom of the film to the top.[31] A second possible structure is a double cermet which consists of two layers of a low metal volume fraction (LMVF) layer deposited on a high metal volume fraction (HMVF) layer.[25] The schematic of these two structures depicted in Fig. 6 and 7 offer greater flexibility and potentially higher performance.
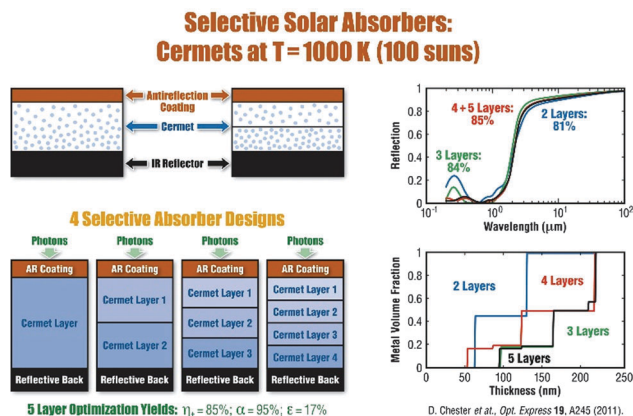
Fig. 7 Design and performance of a selective solar surface based on cermets (tungsten and alumina nanocomposites, adapted from Chester, 2011[27]).

The highest performance designs that have been built and tested to date are multilayer ceramic and metal nanocomposites, known as cermets.[32,33] Their performance and behaviour can be understood as an extension of multilayer ceramic and metal macrocomposite layers. Furthermore, several research papers over the last few years have suggested even further improvements are possible with carefully-designed multilayer cermets.[34,35] Preliminary modelling data suggests that cermets with rugate filters, with roughness on a micron scale, can achieve a tripartite division of the solar spectrum at high temperatures (above 1000 K) and efficiencies. Fig. 7 demonstrates the designs and corresponding maximum predicted maximum performance of 85% solar-to-thermal capture at 500 Suns.[27]

In all selective solar absorbers, thermal stability is a key consideration. Very recent work has demonstrated that other types of materials, such as black oxides, may also offer high temperature stability (up to 750 C under 1000 Suns), with sufficient solar thermal efficiency to be an attractive alternative.[36]

2.3. Solar thermoelectrics

For the thermal power generation component of this system, one can consider utilizing a revolutionary approach to demonstrating high temperature, robust thermoelectric systems with excellent potential for low cost integration into topping cycle applications. The topping thermoelectric generator uses a temperature above the practical highest steam temperature for the bottoming Rankine cycle generator. With the use of scalable microfabrication techniques, thermoelectric modules with thousands of elements can be fabricated. Taking advantage of higher heat flux by concentrating the heat through thermoelectric legs and co-optimizing advanced heat exchangers will ensure larger power output, mechanical robustness under large temperature cycling, and low material cost. Although it can be difficult to achieve a balance between the thermal insulation and electrical conduction needed for thermoelectrics to work well, significant progress has been made in recent years.[37]

In the thermal co-generation approach, we optimize the TE module for highest efficiency at maximum output power (and not for maximum efficiency).[38] This gives the highest W kg^{-1}

and lowest \$ W^{-1} for the system. In this case, the thermal impedance of the TE leg should be nearly equal to the total thermal impedances of the heat exchangers as well as other passive components inside the module (TE plates and heat spreaders, interface thermal resistances). There is a misconception that one may want to design TE material to operate *e.g.* between 550 °C and 800 °C (cold and hot reservoir temperatures) for full temperature range. This is not correct. Yazawa *et al.* have shown that at optimum electrothermal co-design, the temperature difference across the TE leg should be only half of the total temperature difference.[39] Due to the link of thermal and electrical resistances, a ΔT that is too large limits the heat flow. Thus we need a TE material which is optimized for $T_{low} \sim 615$ °C, and $T_{high} \sim 735$ °C. This is the case if we assume the thermal resistances of the hot and cold heat exchangers are the same. We can keep the same ΔT of ~ 125 °C and operate the TE leg closer to the hot source temperature or the cold temperature by adjusting the heat exchangers and the optimum TE leg thickness.

Although interest in using thermoelectric (TE) power conversion for high-temperature waste recovery has gained much momentum over the last few years, there is currently almost no large scale application, primarily because of the lack of practical high-temperature TE materials and modules. The only commercially available modules that could be used for waste heat recovery are made out of Bi_2Te_3-based alloys and are limited to temperatures of about 180 °C. This severely limits the use of TE technology for waste heat recovery, since there are a number of potential applications where the temperature could be as high as 2000 °C. Radioisotope Thermoelectric Generators (RTGs) have already powered a number of NASA space missions. They generate electricity by converting the heat released from the nuclear decay of radioactive isotopes (typically plutonium-238) into electricity using a TE converter that operates at a hot-side temperature of about 1000 °C. RTGs have used either lead telluride (PbTe) and tellurides of antimony, germanium, and silver (TAGS) or silicon germanium (SiGe) alloys (up to 1000 °C). System conversion efficiency for state-of-practice RTGs is about 6%, and RTGs have typically used unicouples rather than modules, primarily because of the rather low heat flux generated by the plutonium heat source. A limited number of TE generators are commercially available today. For example, Global Thermoelectric offers TE generators that are typically designed to deliver power for remote, unattended applications. These generators use PbTe-based TE modules ($T_{high} < 500$ °C), thus limiting their efficiency to about 5–6%.

SiGe alloys have also been successfully used in several types of RTGs. Over the last few years, nanostructured composites of p-type and n-type SiGe and Si have been developed, which can be synthesized using a ball milling process. The best ZT values achieved to date for these materials are on the order of 0.6–1.0. Nanostructuring improved ZT values by up to $\sim$60%. Aging studies have been conducted for p-type and n-type $Si_{80}Ge_{20}$ alloys and it has been shown that the thermal conductivity remained constant (*i.e.* no grain growth) after up to 13 months of testing.[40] We already know that the utilizing thermoelectric legs with a small fractional area of about 10% of the overall foot

print, significantly reduces the mass use of the material (nearly two orders of magnitude).[41] Hence the relatively expensive materials for the thermoelectric legs will not significantly impact the overall cost.

Best performance for the proposed TE module can be achieved through a combination of analytical modelling, numerical simulations, and experimentation, wherein the mechanical robustness of the proposed TE module is co-optimized with its thermal and electrical performance. Thermal loading caused by the different and variable temperatures of the TE module's "hot" and "cold" substrate plates dominates intrinsic mechanical failures in such a system.[42]

Stress is induced by the temperature gradient in the module structure, which results in thermal expansion or contraction mismatches between dissimilar materials. Major stresses include normal stresses acting in the cross-sections of the substrate, as well as shearing and peeling stresses acting at the material interfaces. Based on early work on assemblies with inhomogeneous bonding layers,[43] and more recent investigations,[20,22] the maximum interfacial shearing stress is the most crucial thermal stress to be evaluated and minimized to improve module robustness. One should consider both short-term strength and long term fatigue strength. The short-term strength has to do with the ability of the module structure to withstand high thermal loading that is applied just once to the structure, while its fatigue strength is determined by the ability of the design to successfully sustain prolonged repetitive and relatively low level loading over its lifetime.

In our previous work,[41,44] we obtained an analytic expression for the interfacial shearing stress in a simplified TE module. It has been shown that a small fill factor and thicker legs would result in a significant stress relief in the interfacial shearing stress. It has also been shown that stress relief could be achieved even if shorter legs are employed, provided that the legs are thin enough, and the spacing between the legs is significant. It is imperative, of course, that if small fill factor legs are employed for lower stresses that there is still enough interfacial "real estate", so that the adhesive strength of the assembly is not compromised. The results obtained on the basis of analytical modelling are in good agreement with the preliminary FEA predictions. In the calculations carried out, as an example, Fig. 8 shows a five-legged module design (top) for the high-temperature power generator with SiGe. The numerical simulation result (bottom) shown here is based on a 2D model. We will explore more detail the 3D influences for specific high temperature ranges, with the materials SiGe for TE and molybdenum for the substrate. These have a small CTE mismatch. This combination is considered for its long-term reliability advantage. To minimize the stress, which is primarily shear-stress near the leg interfaces, the metallization (copper) thickness and the molybdenum substrate thickness needs to be as small as possible without increasing parasitic resistances, such as heat spread resistances or series electrical interconnect resistances. They still however, need to be sufficiently thick to handle. For example, if the optimum TE leg thickness is 500 μm with 10% fill factor, it is suggested that the metallization be 30–50 μm and the molybdenum substrate plate be 100 μm.

A key innovation is the use of a relatively low temperature commercial wafer bonding technique to attach the module
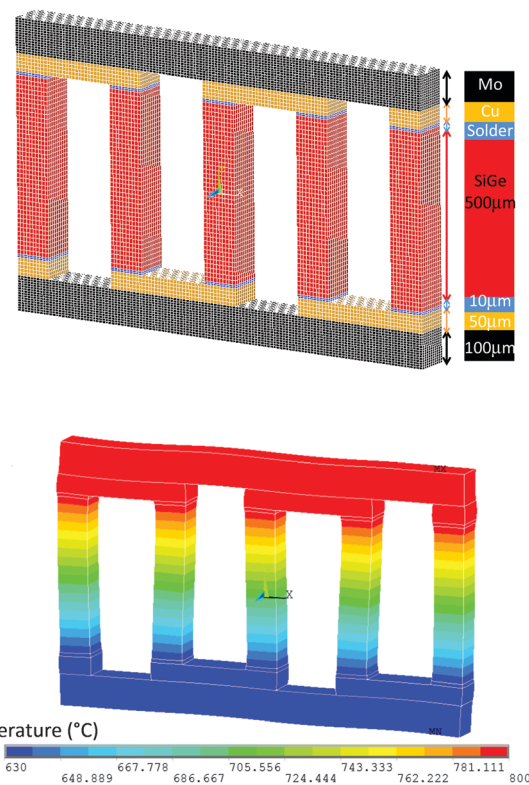

Fig. 8 Thermomechanical 2D simulation for a 5-leg TE module in ANSYS. The TE material is SiGe, and the substrates are Molybdenum. The largest stress at interfaces is on the order of 56 MPa (ΔT = 170 °C) in shear stress (horizontal-direction). In a real module, there should be an electrical insulation layer at the contact of copper metallization and molybdenum (not shown).

plates and the array of TE legs (see Fig. 8 and 9). Thus centimeter-scale modules with 1000s of elements can be fabricated all at once with micron scale alignment resolution. Diffusion barriers and brazing material will be deposited on the TE wafer prior to the bonding. Subsequently, high temperatures and/or pressures will be used to form the brazing bonds that are stable at temperatures > 800 °C. This approach is suited to mass production at low cost.

We have previously fabricated 400 element generator modules using 10 and 20 μm ErAs:(InGaAs)$_{1-x}$(InAlAs)$_x$ using standard IC processing technology.[45,46] The generator modules were characterized by real device measurements and theoretical device modelling to get a better understanding of the performance for future enhancements.

All thin-film generator modules start with the wafer scale fabrication of the element arrays. The area size of each element array is 6 mm × 6 mm. Each element array chip contains 200 elements. The element size is 120 μm × 120 μm. The mesa height of each element for 10 μm ErAs:(InGaAs)$_{1-x}$(InAlAs)$_x$ is about 12 μm, and over 22 μm for 20 μm ErAs:(InGaAs)$_{1-x}$(InAlAs)$_x$. The element mesa formation is done by using an inductive coupled plasma (ICP) dry etching technique. Fig. 9 shows six whole element array chips that were fabricated on a quarter of a two inch wafer. The n-type and p-type element array chips will be bonded to metal
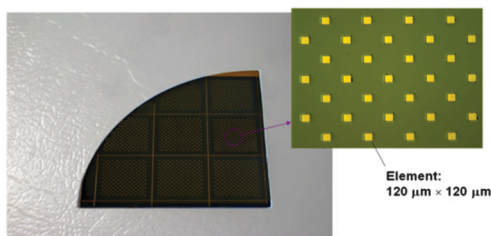
Fig. 9 Six full element array chips were fabricated on the quarter wafer. Each element array chip contains 200 elements, and the area size of each element is 120 μm × 120 μm.

pads on the bottom and top ceramic plates, respectively, using a flip-chip bonding technique. After the InP substrate was removed by wet etching, the bottom plate contains 200 n-type elements and the top plate contains 200 p-type elements as shown in Fig. 10. When 20 μm thick elements were used, a power density of 2.7 W cm^{-2} was achieved ($\Delta T \sim 120$ °C).

A Z-meter is an apparatus that can simultaneously measure the three thermoelectric material parameters on one sample in the same direction, and thus measure ZT directly as a function of temperature. We have built a Z-meter based on the design from the Ram group at MIT,[47] which is capable of measuring the thermoelectric energy conversion efficiency and the power density of a single TE leg as thin as 120 μm. The highest operating temperature was 600 °C, but further upgrades approaching 1000 °C are possible. The performance of thermoelectric modules relies on the material properties as well as the quality of element interconnections and thermal interfaces. Defects may be introduced from the fabrication processing and thermal cycling, which degrades the efficiency and functionality of the thermoelectric module. Electrical and optical imaging tests are essential for enabling a quick 'try and error process' for the design-fabrication-test cycle. TE module design optimization shall be done by modelling. However, the true reliability must be proven by cyclic testing. Major defects are typically connected with an increase of electrical impedance which may occur with parasitic resistance and/or capacitance somewhere in the series circuit. Manufacturing defects change the thermal power distribution so high resolution thermal imaging is essential. In the lab, we use the thermoreflectance
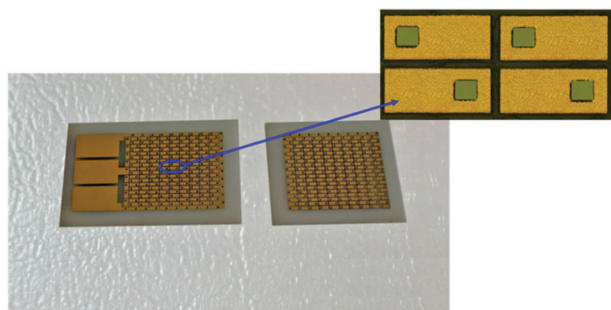

Fig. 10 400 elements of 200 n-ErAs:InGaAlAs and 200 p-ErAs:InGaAs elements, 10 μm thick, were bonded on the upper and lower AlN plates *via* wafer scale approach and flip-chip bonding technique.
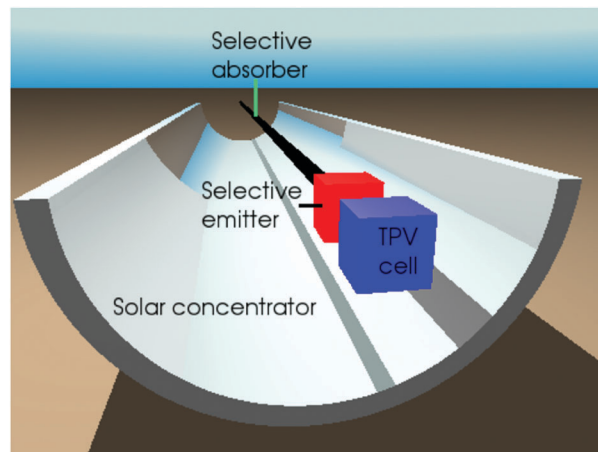

Fig. 11 Schematic diagram of a solar TPV system, which concentrates sunlight onto a selective absorber to generate heat. This heat is fed into a selective emitter, which radiates onto a low-bandgap TPV cell to generate electricity (adapted from ref. 51).

technique to obtain thermal images inside the thermoelectric packages.[48]

2.4. Solar thermophotovoltaics

A solar thermophotovoltaic (TPV) system is a variation on the standard TPV system, illustrated in Fig. 11, in which optical concentrators, such as parabolic mirrors or Fresnel lenses, are used to concentrate sunlight onto a selective absorber and emitter structure.[49] The selective absorber, similar to those used for solar water heaters and solar thermal mechanical generation, is thermally coupled to a selective emitter, which generates thermal photons. These illuminate a low-bandgap photovoltaic (PV) cell, generating electricity.[50]

Thus, solar TPV uses sunlight as a heat source to perform electrical work. It is clear that the two parts of the overall solar thermal TPV system – the optical concentrator and selective absorber subsystem and the selective emitter and TPV cell subsystem – can be conceptually decoupled, with the output of the solar absorber serving as input to the TPV component. Furthermore, as solid-state devices, they have the potential for higher reliability, vastly smaller form factors (meso- and microscales), and higher energy densities than traditional mechanical engines.

3. Hybrid solar cogeneration strategies

3.1. Hot photovoltaics

Running photovoltaic cells at elevated temperatures has the potential for the productive use of excess thermal energy. The maximum power produced by the combined photovoltaic and thermal system can be measured in terms of exergy, which consists of electric power plus a de-rated thermal power contribution, where the de-rating factor is known as the Carnot factor, which reflects the maximum efficiency at which one could potential convert thermal energy to electricity. The Carnot factor is given by $1 - T_c/T_h$, where T_c is the cold temperature
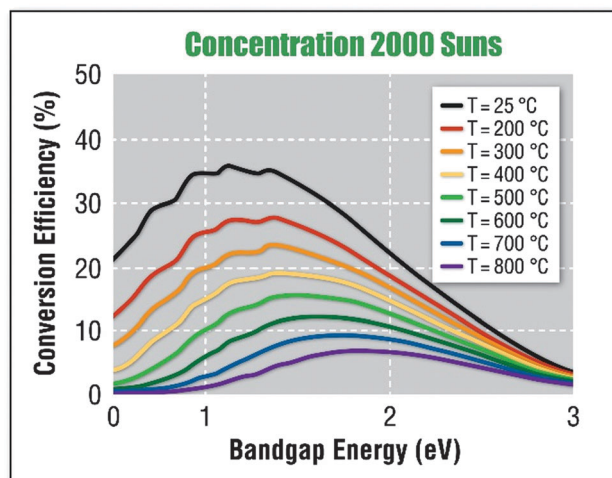
Fig. 12 Maximum conversion efficiency *versus* bandgap and temperature found for PV model from this proposal. The rapid decline in efficiencies above 100 °C should be avoided.

reservoir (typically room temperature), and T_h is the hot-side thermal input. The actual realized efficiency will then be bounded from above by the exergy, which is given by:

$$\eta = \eta_{pv} + (1 - \eta_{pv})\eta_{me}, \qquad (6)$$

where η_{pv} is the PV conversion efficiency, and η_{me} is the realized mechanical conversion efficiency. At modest temperatures up to 550 °C, the mechanical conversion efficiency will typically be 2/3 or less of the Carnot limit. The PV conversion efficiency varies with bandgap, and is therefore not as straightforward to calculate; however, this calculation can be done using the

expressions from Section 2.1. The results are presented in Fig. 12. We find that as temperatures increase above room temperature, efficiencies decline rapidly. For example, increasing the temperature to 400 °C decreases maximum efficiency by 17%; at the same time, the remaining contribution from cogeneration is limited to 30% under ideal circumstances. As a result, adding thermal cogeneration has the potential to improve overall performance. However, as will be shown in the next section, adding an additional topping cycle made of thermoelectrics can lead to greater conversion efficiency than this approach alone.

3.2. Solar PV/thermoelectric/mechanical

3.2.1 Spectrum splitting. Our proposed concept, originally presented schematically in Fig. 1, is illustrated in greater detail in Fig. 13. Designing the selective solar reflector/absorber, high temperature heat exchanger, low stress integration, and optimizing the overall system are the keys to properly partitioning incoming solar power between the PV, TE, and mechanical subsystems.

3.2.2 High bandgap PV cell. In order to make the best possible use of high-energy photons, one or more high bandgap photovoltaic cells will be needed. In contrast with traditional single or multijunction designs, the emphasis here is not on achieving maximum conversion efficiency over the entire solar spectrum, but rather, over a designated subset exclusively in the visible spectrum. To that end, wide bandgap III–V cells offer a solution supported by a great deal of recent work. In particular, it can be shown that nearly lattice-matched tandem junction systems, consisting of two separate bandgaps of 1.7 eV and 2.2 eV, would yield the best performance over the designated range of high energy photons suitable for this spectral-splitting approach. One potential material system to achieve this combination would be indium aluminum arsenide (InAlAs) on indium gallium phosphide (InGaP). The key challenge with this system is the presence of hygroscopic aluminum in the upper layer that
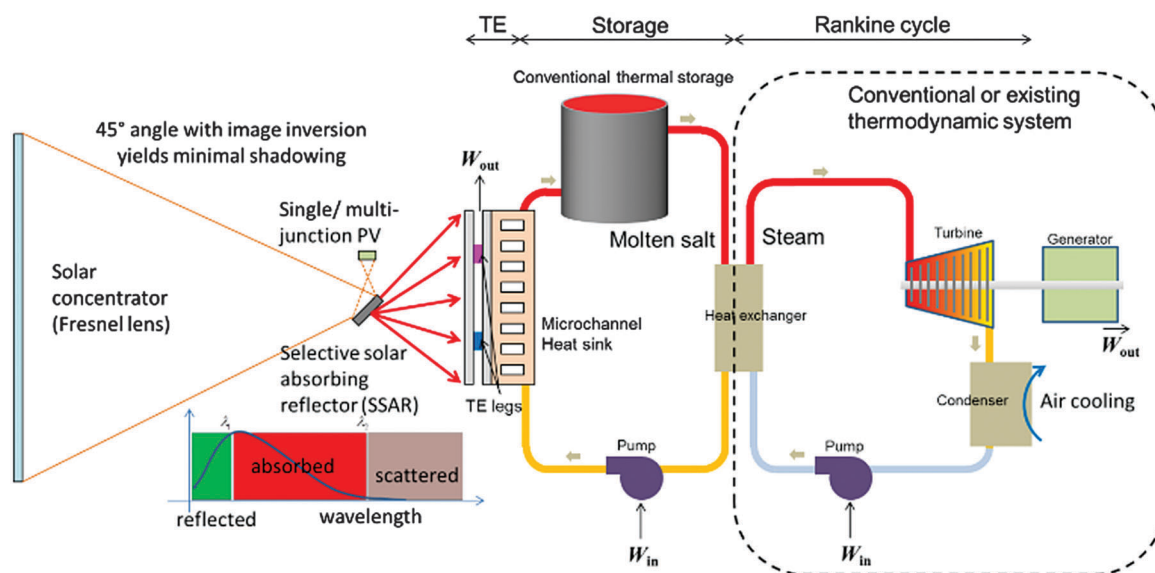

Fig. 13 Basic concept: (a) block diagram illustrating the key components combined by our approach; and (b) detailed diagram depicting its proposed experimental implementation.

could potentially lead to degradation in the external quantum efficiency under operating conditions. Special encapsulation approaches, such as packing with room-temperature phase change materials like polyolefins, may help prevent any moisture ingress and subsequent loss of EQE.

3.2.3 TE and heat sink optimum design as a thermal topping cycle.
After splitting the solar spectrum, incoming heat flux is assumed to be 1.9×10^5 W m^{-2} at 800 °C with 500× optical concentration. Another constraint is the steam temperature of 550 °C for the heat sink and thermal storage design. As discussed in Section 2.3, the thermoelectric modules are designed to match the maximum power output. The cold side heat sink must satisfy the above heat flux and the temperature delta, approximately 125 °C. The effective heat transfer coefficient must be $1.5 \times 10^{+3}$ W m^{-2} K^{-1} for the contact between the thermoelectric and the heat sink. Recently-developed electronics cooling technology with mini- or micro-channel heat sinks can easily provide the required heat transfer coefficient.

There are two major approaches to realizing both heat transport and storage, based on using molten salt and supercritical steam, respectively, as the working fluids. Using molten salt as the working fluid is popular for large scale solar concentrated tower and mechanical (steam turbine) systems. The composition of the material can be found from wide variations of working temperature range and other properties. Considering the high heat flux, the viscosity of the molten salt is a key selection criterion. Some molten salts have water-like viscosities, thus the pump will not be a big issue. Thermal conductivity of the molten salt at the operating temperature is also considered to be not too low compared to the water at room temperature. Storing the heat is simply buffering the hot molten salt and using another heat exchanger to supply heat to the steam.

Using super critical steam as the working fluid is another potential approach. At the heat sink, the steam would receive the heat in the super critical fluid with pressure over 22 MPa, since the temperature already exceeds the critical temperature. The performance of heat transport is worse than in the liquid phase, but better than the vapour phase. The challenge that arises here, is the high pressure proof design of the heat sink and the piping. To alleviate this challenge, it may be better to use molten salt as the thermal storage medium, accessed *via* heat exchangers.

We assume the conventional trans-critical steam Rankine cycle without changing any of the technical specifications for the generators. The system scale is determined by the available capacity of the steam turbines. It is interesting that increasing dispatchability requirements can help decrease turbine generator power requirements (relative to the scale of solar collector). For example, in order to achieve 50% dispatchability, only half of the power generating capacity is required for the steam turbine, compared to full-time operation.

To handle the high heat flux exiting the cold side of thermoelectric module, a microchannel heat sink may be required. The thermal resistance of this heat sink is an important key for the performance of thermoelectric power generation as well as

minimizing additional pump power due to the flow resistance in the microchannel heat sink. Thermo-fluidic consideration and co-optimization were studied in our previous work.[39]

3.2.4 System efficiency and dispatchability.
The overall performance of our system can be represented as follows:

$$\eta = \eta_{pv} + (1 - \eta_{pv})\eta_{ssar}[\eta_{te} + (1 - \eta_{te})\eta_{me}], \qquad (7)$$

where η_{ssar} is the fraction of total incident solar radiation absorbed as heat by the selective solar absorbing reflector (SSAR); η_{te} is the thermoelectric component efficiency; η_{pv} is the photovoltaic component efficiency using the reflected light, which cannot exceed $1 - \eta_{ssar}$; and η_{me} is the mechanical engine conversion efficiency.

Fig. 14 above provides the overall attainable system efficiency and maximum fraction of dispatchable energy for a tandem-junction PV cell with a bandgap E_g, specified on the x-axis, and a selective solar absorber under 1000 Suns illumination, operating at a hot-side temperature T_{ssar}, specified by the y-axis. Nonetheless, more work is needed to show the commercial applicability of this approach. The thermal components consist of a thermoelectric and a Rankine cycle connected at 550 °C; the cooling water temperature at the condenser is given as 37 °C. The efficiency of the Rankine cycle is taken to be 2/3 of the
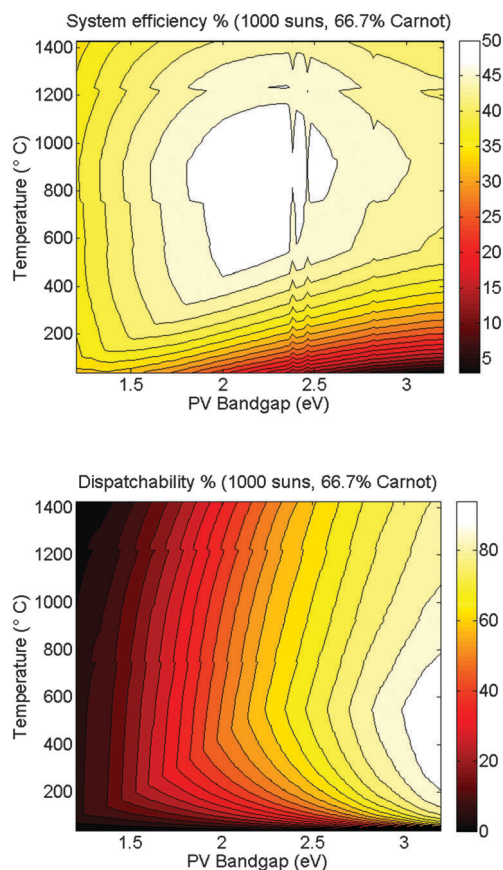

Fig. 14 (top) System efficiency limits and (bottom) dispatchable energy fraction as a function of PV bandgap and selective solar absorbing reflector operating temperature, using tandem-junction PV, TE with ZT = 1, and a mechanical engine operating at 2/3 of the Carnot limit.

Carnot efficiency. The maximum system efficiency is found to be 50% (with $ZT = 1$ at 900 °C). This can be achieved using tandem PV bandgaps of 1.7 and 2.2 eV (using, *e.g.*, InAlAs/InGaP) at 72 °C, and a thermoelectric consisting of a ErAs:$(InGaAs)_{1-x}(InAlAs)_x$, operating at a hot-side temperature of approximately 1000 °C. With reasonable thermal energy storage (TES), up to 63% of peak power is dispatchable and sufficient to maintain power generation throughout the day with only 1.5% energy loss through the advanced insulation of the tank wall.

The resulting improvement in efficiency from using our system is immense, yielding potential system efficiencies up to 50% using individual components under experimentally-tested operating conditions, with LCOEs as low as $0.06 per kW per h with 63% dispatchability. This compares quite favourably with a record efficiency of 44% for PV multi-junction cells (no dispatchability) and ~15% achieved with state-of-the art thermoelectrics.

One may ask about rationale for including the thermo-electric (TE) stage given an efficiency of only 5%. We have presented a novel concept that is only at the beginning of its learning curve. Without the TE module, one could optimize the selective solar surface and the PV cell to achieve an overall system exergy of 47% (see Fig. 15). This is a great achievement, however, the performance of the system without TE will be towards the end of its learning curve since this involves
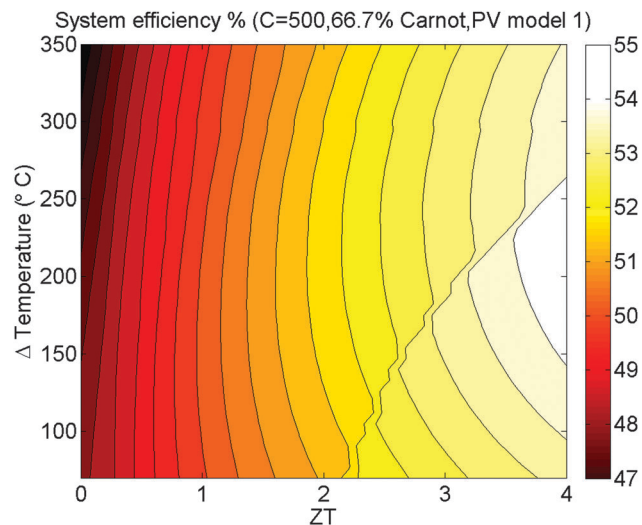
Fig. 16 Calculated system exergy as a function of the selective solar surface (SSS) temperature differential (75–350 °C) and the ZT value of the thermo-electrics. We assumed 500× solar concentration. As one goes from no thermo-electrics to $ZT = 4$, an overall improvement of 8% can be achieved. These calculations take into account re-radiation losses at high SSS temperatures.

Rankine cycles and standard multijunction PVs that have been optimized for many years. On the other hand, introducing new TE materials opens up the potential to approach exergies of 54% with $ZT = 3.6$ (see Fig. 16).

There has been a renewed interest in TEs in the last 10–15 years, but there are no commercial-large scale TE waste heat recovery applications yet. Even though this is all solid-state technology without moving parts, and radioisotope thermal generators (RTGs) have demonstrated 30 year lifetime in space, it will be a challenge to scale. TE generators as a topping cycle have the potential to be one of the first large-scale implementation of this technology. This is because TE modules can work at a tempera-ture range (>550 °C) where mechanical systems have a hard time competing with significantly higher performance, due to challenges in transport. There are high-temperature Rankine and Brayton cycles engines but the cost has been prohibitive despite many years of research. A key factor limiting efficiency of TE modules is the heat leakage from the hot to the cold side through the TE material. As a topping cycle, the heat at the cold side is not wasted, but is used to run the bottom Rankine cycle.

One has to emphasize that calculations are performed for TE topping cycle employing a temperature gradient of 250 °C. This is significantly lower than 500–700 °C used in automotive exhaust or in space RTG applications. The maximum output power of thermoelectric module is proportional to the square of the temperature gradient. In the current analysis, one does not get as much power from the TE module but the thermally induced stress issues are much more manageable. Later on, one could focus on using higher performance TE materials ($ZT \approx 2.2$ at 600 °C has been demonstrated, and theoretical calculations show that $ZT \approx 4$ is possible). One could also increase the temperature on the hot side of the TE module. Doubling the temperature gradient across TE can quadruple the output power from TE. As shown in Fig. 16, however, there
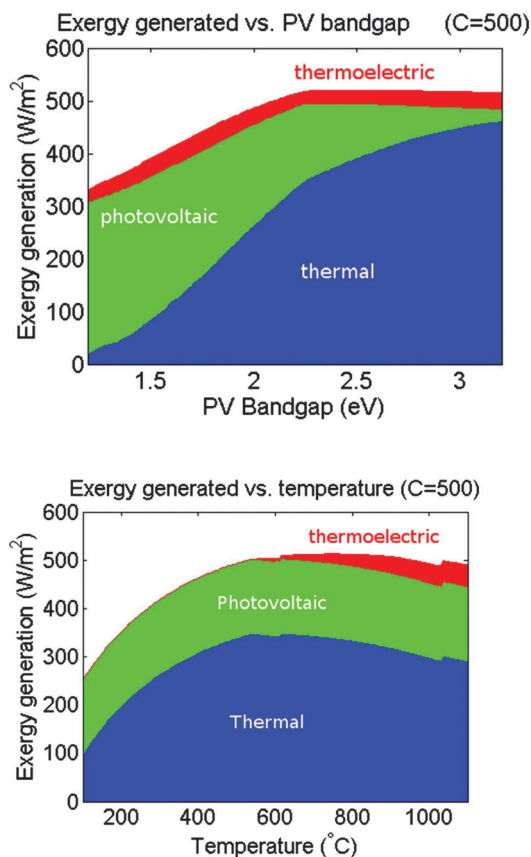

Fig. 15 (top) Contributions to exergy generation as a function of PV bandgap at a constant solar absorber temperature of 800 °C. (bottom) Contributions to exergy generation as a function of solar absorber tem-perature at a fixed PV bandgap of 2.2 eV.

are significant re-radiation losses that are included in the overall system modelling. More could be done to suppress re-radiation, such as introducing angular selectivity and using higher solar concentration. This can be considered an opportunity for improvement and the basis of new learning curves in the future.

4. Conclusions and future work

Our hybrid approach brings together three distinct technologies, photovoltaics, thermoelectrics, and Rankine cycle turbines, under a common system framework to enable the full spectrum of sunlight to be converted into electricity with much higher efficiency and dispatchability than existing solutions at an affordable price on a utility scale. The primary rationale for our approach is that each technology has strength in complementary regimes, and our suggested division of photonic and thermal power utilizes each technology in the best way possible. When operational, such a system could provide baseload or daytime utility-scale power, or it could be utilized in local micro grids in less populated areas. Also, industrialization of the key components would promote the creation of domestic jobs to assemble the associated cost-effective renewable source power generation systems. Before this approach can be fully implemented, major breakthroughs are still required in the selective absorber and in reliable high temperature thermoelectric modules. Minimizing thermal losses at various interfaces, integration with the high temperature heat exchangers and thermal stress reduction in the entire structure are other major challenges that warrant further study.

Acknowledgements

References

1 D. Feldman, G. Barbose, R. Margolis, R. Wiser, N. Darghouth, A. Goodrich, Photovoltaic (PV) Pricing Trends: Historical, Recent, and Near-Term Projections. Technical Report DOE/GO-102012-3839, 2012.

2 K. Park, S. Shin, A. Tazebay, H. Um, J. Jung, S. Jee, M. Oh, S. Park, B. Yo, C. Yu and J. Lee, Lossless hybridization between photovoltaic and thermoelectric devices, Sci. Rep., 2013, 3, 2123, DOI: 10.1038/srep02123.

3 D. Kraemer, L. Hu, A. Muto, X. Chen, G. Chen and M. Chiesa, Photovoltaic-thermoelectric hybrid systems: a general optimization methodology, Appl. Phys. Lett., 2008, 92, 243503, DOI: 10.1063/1.2947591.

4 N. Wang, L. Han, H. He, N. Park and K. Koumoto, A novel high-performance photovoltaic–thermoelectric hybrid device, Energy Environ. Sci., 2011, 4, 3676–3679.

5 T. Chen, G. Guai, C. Gong, W. Hu, J. Zhu, H. Yang, Q. Yan and C. Li, Thermoelectric Bi_2Te_3-improved charge collection for high-performance dye-sensitized solar cells, Energy Environ. Sci., 2012, 4, 6294–6298.

6 S. Shin, J. Jung, M. Park, J. Song and J. Lee, Catalyst-free hydrogen evolution of Si photocathode by thermovoltage-driven solar water splitting, J. Power Sources, 2015, 279, 151–156.

7 A. Imene and D. Mills, Spectral beam splitting technology for increased conversion efficiency in solar concentrating systems: a review, Sol. Energy Mater. Sol. Cells, 2004, 84, 19–69.

8 J. Zhengshan, K. Fisher, B. Wheelwright, R. Angel and Z. Holman, PVMirror: a new concept for tandem solar cells and hybrid solar converters, IEEE J. Photovol., 2015, 5, 1791–1799.

9 F. Crisostomo, R. Taylor, T. Zhang, I. Perez-Wurfl, G. Rosengarten, V. Everett and E. Hawkes, Experimental testing of SiN_x/SiO_2 thin film filters for a concentrating solar hybrid PV/T collector, Renewable Energy, 2014, 72, 79–87.

10 C. H. Henry, Limiting efficiencies of ideal single and multiple energy gap terrestrial solar cells, J. Appl. Phys., 1980, 51, 4494–4500.

11 W. Guter, J. Schöne, S. Philipps, M. Steiner, G. Siefer, A. Wekkeli, E. Welser, E. Oliva, A. Bett and F. Dimroth, Current-matched triple-junction solar cell reaching 41.1% conversion efficiency under concentrated sunlight, Appl. Phys. Lett., 2009, 94, 223504.

12 W. Wu, B. Lei, H. Rao, Y. Xu, Y. Wang, C. Su and D. Kuang, Hydrothermal fabrication of hierarchically anatase TiO_2 nanowire arrays on FTO glass for dye-sensitized solar cells, Sci. Rep., 2013, 3, 1352, DOI: 10.1038/srep01352.

13 M. He, X. Pang, X. Liu, B. Jiang, Y. He, H. Snaith and Z. Lin, Monodisperse Dual-Functional Upconversion Nanoparticles Enabled Near-Infrared Organolead Halide Perovskite Solar Cells, Angew. Chem., 2016, 28, 4352–4356, DOI: 10.1002/ange.201600702.

14 M. He, J. Ge, Z. Lin, X. Feng, X. Wang, H. Lu, Y. Yang and F. Qiu, Thermopower enhancement in conducting polymer nanocomposites via carrier energy scattering at the organic–inorganic semiconductor interface, Energy Environ. Sci., 2012, 5, 8351–8358.

15 M. A. Green, K. Emery, Y. Hishikawa, W. Warta and E. D. Dunlop, Solar cell efficiency tables (version 40), Prog. Photovoltaics, 2012, 20, 606–614.

16 J. R. Wilcox, Solar Cell Temperature Dependent Efficiency and Very High Temperature Efficiency Limits, PhD thesis, Purdue University, West Lafayette, IN, 2013.

17 J. L. Gray, A. W. Haas, J. R. Wilcox and R. J. Schwartz, Efficiency of Multijunction Photovoltaic Systems, Proc. IEEE Photovolt. Spec. Conf., 2008, 33, 1–6, DOI: 10.1109/PVSC.2008.4922911.

18 W. Shockley and H. J. Queisser, Detailed Balance Limit of Efficiency of p–n Junction Solar Cells, J. Appl. Phys., 1961, 32, 510–519.

19 J. L. Gray, J. Schwarz, J. R. Wilcox, A. W. Haas and R. J. Schwartz, Peak efficiency of multijunction photovoltaic systems, Proc. IEEE Photovolt. Spec. Conf., 2010, 35, 2919–2923, DOI: 10.1109/PVSC.2010.5615827.

20 J.-L. Gao, Q.-G. Du, X.-D. Zhang and X.-Q. Jiang, Thermal Stress Analysis and Structure Parameter selection for a Bi_2Te_3-based Thermoelectric Module, *J. Electron. Mater.*, 2011, **40**, 884–888.

21 J. L. Gray and J. R. Wilcox, The Design of Multijunction Photovoltaic Systems for Realistic Operating Conditions, (Invited Paper), *Proc. IEEE Internat. Midwest Symp. Circuits Syst.*, 2013, **56**, 697–700.

22 E. E. Antonova and D. C. Looman, Finite Elements for Thermoelectric Device Analysis in ANSYS, *Proc. ICT Internat. Conf. Thermoelectr.*, 2005, **24**, 215–218.

23 Q. Zhang, High efficiency Al–N cermet solar coatings with double cermet layer film structures, *J. Phys. D: Appl. Phys.*, 1999, **32**, 1938–1944.

24 P. Bermel, J. W. Lee, I. Celanovic, J. D. Joannopoulos and M. Soljacic, *Annual Review of Heat Transfer XV*, Begell House, Reading, CT, 2012.

25 Q. Zhang, K. Zhao, B. Zhang, L. Wang, Z. Shen, D. Lu, D. Xie and B. Li, High performance Al–N cermet solar coatings deposited by a cylindrical direct current magnetron sputter coater, *J. Vac. Sci. Technol., A*, 1999, **17**, 2885–2890.

26 P. Bermel, M. Ghebrebrhan, W. R. Chan, Y. X. Yeng, M. Araghchini, R. Hamam, C. H. Marton, K. F. Jensen, M. Soljacic, J. D. Joannopoulos, S. G. Johnson and I. Celanovic, Design and global optimization of high-efficiency thermophotovoltaic systems, *Opt. Express*, 2010, **18**, A314–A334.

27 D. Chester, P. Bermel, J. D. Joannopoulos, M. Soljacic and I. Celanovic, Design and global optimization of high-efficiency solar thermal systems with tungsten cermets, *Opt. Express*, 2011, **19**, A245–A257.

28 A. Donnadieu and B. O. Seraphin, Optical performance of absorber-reflector combinations for photothermal solar energy conversion, *J. Opt. Soc. Am.*, 1978, **68**, 292–297.

29 M. Okuyama, K. Saji, T. Adachi, H. Okamoto and Y. Hamakawa, Selective absorber using glow-discharge amorphous silicon for solar photothermal conversion, *Sol. Energy Mater.*, 1980, **3**, 405–413.

30 C. E. Kennedy, *Review of Mid- to High Temperature Solar Selective Absorber Materials*, National Renewable Energy Laboratory Research Report, Golden, Colorado, 2002.

31 T. S. Sathiaraj, R. Thangaraj, H. Al Sharbaty, M. Bhatnagar and O. P. Agnihotri, $Ni:Al_2O_3$ selective cermet coatings for photothermal conversion up to 500 °C, *Thin Solid Films*, 1989, **190**, 241–254.

32 F. Cao, D. Kraemer, L. Tang, Y. Li, A. Litvinchuk, J. Bao, G. Chen and Z. Ren, A high-performance spectrally-selective solar absorber based on a yttria-stabilized zirconia cermet with high-temperature stability, *Energy Environ. Sci.*, 2015, **8**, 3040–3048.

33 L. Rebouta, A. Sousa, P. Capela, M. Andritschky, P. Santilli, A. Matilainen, K. Pischow, N. Barradas and E. Alves, Solar selective absorbers based on Al_2O_3: W cermets and AlSiN/AlSiON layers, *Sol. Energy Mater. Sol. Cells*, 2015, **137**, 93–100.

34 F. Cao, K. McEnaney, G. Chen and Z. Ren, A review of cermet-based spectrally selective solar absorbers, *Energy Environ. Sci.*, 2014, **7**, 1615–1627.

35 S. Wu, C. Cheng, Y. Hsiao, R. Juang and W. Wen, Fe_2O_3 films on stainless steel for solar absorbers, *Renewable Sustainable Energy Rev.*, 2016, **58**, 574–580.

36 T. Kim, B. VanSaders, E. Caldwell, S. Shin, Z. Liu, S. Jin and R. Chen, Copper-alloyed spinel black oxides and tandem-structured solar absorbing layers for high-temperature concentrating solar power systems, *Sol. Energy*, 2016, **132**, 257–266.

37 G. Snyder and E. Toberer, Complex thermoelectric materials, *Nat. Mater.*, 2008, **7**, 105–114.

38 K. Yazawa and A. Shakouri, Optimization of power and efficiency of thermoelectric devices with asymmetric thermal contacts, *J. Appl. Phys.*, 2012, **111**, 024509.

39 K. Yazawa and A. Shakouri, Cost-Efficiency Trade-off and the Design of Thermoelectric Power Generators, *Environ. Sci. Technol.*, 2011, **45**, 7548–7553.

40 J. W. Vandersande, J. P. Fleurial, N. Scoville, J. L. Rolfe, Thermal Conductivity Reduction in p-type $Si_{80}Ge_{20}$ Alloys due to Ultrafine BN Particulates, JPL Technical Report, 1993.

41 E. Suhir and A. Shakouri, Assembly Bonded at the Ends: Could Thinner and Longer Legs Result in a Lower Thermal Stress in a Thermoelectric Module (TEM) Design?, *J. Appl. Mech.*, 2012, **79**, 061010, DOI: 10.1115/1.4006597.

42 E. Suhir, Stresses in Bi-Metal Thermostats, *J. Appl. Mech.*, 1986, **53**, 657–660.

43 E. Suhir, Thermal Stress in a Bi-Material Assembly with a 'Piecewise-Continuous' Bonding Layer: Theorem of Three Axial Forces, *J. Phys. D: Appl. Phys.*, 2009, **42**, 045507.

44 E. Suhir and A. Shakouri, Predicted Thermal Stresses in an Assembly with an Inhomogeneous Bond, and with Application to a Multi-Leg Thermoelectric Module (TEM) Design, *J. Appl. Mech.*, 2013, **80**, 021012.

45 G. Zeng, J.-H. Bahk, J. E. Bowers, J. M. O. Zide, A. C. Gossard, Z. Bian, R. Singh, A. Shakouri, W. Kim, S. L. Singer and A. Majumdar, $ErAs:(InGaAs)_{1-x}(InAlAs)_x$ alloy power generator modules, *Appl. Phys. Lett.*, 2007, **91**, 263510.

46 G. Zeng, J.-H. Bahk, J. E. Bowers, H. Lu, J. M. O. Zide, A. C. Gossard, R. Singh, Z. Bian, A. Shakouri, S. L. Singer, W. Kim and A. Majumdar, Power Generator Modules of Segmented Bi_2Te_3 and $ErAs:(InGaAs)_{1-x}(InAlAs)_x$, *J. Electron. Mater.*, 2008, **37**, 1786–1792.

47 R. Amatya, P. M. Mayer and R. J. Ram, High temperature Z-meter setup for characterizing thermoelectric material under large temperature gradient, *Rev. Sci. Instrum.*, 2012, **83**, 075117.

48 R. Singh, J. Nurnus, Z. Bian, J. Christofferson and A. Shakouri, Temperature Profile Inside Microscale Thermoelectric Module Acquired Using Near-Infrared Thermoreflectance, *IEEE Trans. Compon. Packag. Technol.*, 2009, **32**, 447–452.

49 W. Spirkl and H. Ries, Solar thermophotovoltaics: an assessment, *J. Appl. Phys.*, 1985, **57**, 4409–4414.

50 B. D. Wedlock, Thermo-photo-voltaic energy conversion, *Proc. IEEE*, 1963, **51**, 694–698.

51 P. Bermel, W. R. Chan, Y.-X. Yeng, J. D. Joannopoulos, M. Soljacic and I. Celanovic, Design and global optimization of high-efficiency thermophotovoltaic systems, *World Conf. Photovolt. Energy Conv.*, 2010, **5**, 1–6.